

Journal Pre-Proof

Influence of prestress on ballistic performance of bi-layer ceramic composite armors: experiments and simulations

Rui Zhang, Bin Han, Lang Li, Zhong-Nan Zhao, Qi Zhang, Qian-Cheng Zhang, Chang-Ye Ni, Tian Jian Lu

PII: S0263-8223(18)34517-3
DOI: <https://doi.org/10.1016/j.compstruct.2019.111258>
Reference: COST 111258

To appear in: *Composite Structures*

Received Date: 14 December 2018
Revised Date: 24 June 2019
Accepted Date: 26 July 2019

Please cite this article as: Zhang, R., Han, B., Li, L., Zhao, Z-N., Zhang, Q., Zhang, Q-C., Ni, C-Y., Jian Lu, T., Influence of prestress on ballistic performance of bi-layer ceramic composite armors: experiments and simulations, *Composite Structures* (2019), doi: <https://doi.org/10.1016/j.compstruct.2019.111258>

This is a PDF file of an article that has undergone enhancements after acceptance, such as the addition of a cover page and metadata, and formatting for readability, but it is not yet the definitive version of record. This version will undergo additional copyediting, typesetting and review before it is published in its final form, but we are providing this version to give early visibility of the article. Please note that, during the production process, errors may be discovered which could affect the content, and all legal disclaimers that apply to the journal pertain.

© 2019 Published by Elsevier Ltd.



Influence of prestress on ballistic performance of bi-layer ceramic composite armors: experiments and simulations

Rui Zhang^{1,2}, Bin Han^{3,4*}, Lang Li^{1,2}, Zhong-Nan Zhao^{1,2}, Qi Zhang³, Qian-Cheng Zhang¹, Chang-Ye Ni^{2,5}, Tian Jian Lu^{2,5*}

¹State Key Laboratory for Strength and Vibration of Mechanical Structures
Xi'an Jiaotong University, Xi'an 710049, China

²State Key Laboratory of Mechanics and Control of Mechanical Structures,
Nanjing University of Aeronautics and Astronautics, Nanjing 210016, P.R. China

³School of Mechanical Engineering, Xi'an Jiaotong University, Xi'an 710049, PR China

⁴Research institute of Xi'an Jiaotong University, Zhejiang, Hangzhou 311215, China

⁵Nanjing Center for Multifunctional Lightweight Materials and Structures (MLMS),
Nanjing University of Aeronautics and Astronautics, Nanjing 210016, P.R. China

Abstract

The effect of prestress on the ballistic performance of bi-layer ceramic composite armors was explored both experimentally and numerically. Three types of target plate with different prestress levels were prepared using the method of shrink-fit, and tested with ballistic experiments. Residual velocity and length of the projectile were recorded and failure mode of each target was examined. A numerical technique was also proposed to explore the penetration process of projectile and the enhancement mechanism of prestress, with the effectiveness of simulation results validated by experimental measurements. Prestressing the ceramic led to more kinetic energy dissipated by plastic deformation and erosion of the projectile, causing more than 25% increase in ballistic limit. The effects of key geometrical parameters - thickness and diameter of ceramic tile - on ballistic limit were systematically explored, and a critical tile thickness for the influence of prestressing on ballistic performance was identified.

Keywords: Ceramic armor; Pre-stress; Ballistic performance; Penetration; Experiment

*Corresponding authors: hanbinghost@mail.xjtu.edu.cn (B. Han), tjlu@nuaa.edu.cn (T.J. Lu).

1. Introduction

While ceramic has been extensively utilized in armor applications, the combination of a ceramic front and a ductile backing leads to great ballistic enhancement [1-5]. Ceramic with low density, high compressive strength and high hardness is more effective to blunt and erode the projectile, while the ductile backing is efficient in absorbing the kinetic energy of debris [6-8]. However, the low toughness and tensile strength of ceramic limit the further improvement of ballistic performance.

It is well known that the strengths of intact and damaged ceramics are both pressure-dependent, increasing with increasing confining pressure [9]. In the presence of sufficiently high confining pressure, a ceramic could even withstand plastic deformation and would not fail in brittle [10, 11]. Sherman *et al.* [12] found a dramatic reduction in damage of alumina tiles when a compressive prestress of 200 MPa was applied, and the damage in the form of radial cracks was reduced while cone cracks were prevented. It has also been reported that conical and radial cracks in ceramics were suppressed by confining pressure [13]. Therefore, it is quite promising to improve the ballistic efficiency of ceramic armor by prestressing the ceramic.

Several attempts have been made to investigate the influence of prestress on the penetration resistance of ceramics. Gassman *et al.* [14] conducted depth of penetration (DOP) tests on alumina tiles under lateral prestress. They found the penetration depth of armor piercing (AP) projectile decreased with increasing prestress level, and the influence of prestress was more significant as tile thickness was increased. However, DOP test results of silicon carbide indicated that the penetration depth of tungsten long rod projectile (LRP) did not decrease monotonically with the increase in prestress [15]. Besides, prestress was found to play an important role in defeating projectile directly at the surface of ceramic and could improve the transition velocity (velocity at which penetration occurs) [16, 17]. Subsequently, the experimental results [16] were used to validate numerical simulation results of the penetration of prestressed ceramic targets under LRP impacts [18]. Holmquist and Johnson [19]

also computed the response of thin encapsulated ceramic target under the impact of steel projectile, but no experimental verification was provided.

Existing experimental researches on prestressed ceramic are almost conducted by DOP tests with semi-infinite thickness ceramic or metal backing, and there is not yet a relevant experimental work on prestressed thin ceramic with thin backing. In addition, the numerical technique to implement prestress is still scarce, making it difficult to explore the penetration mechanism for the prestressed ceramic. We therefore carried out experiments to quantify the influence of prestress on the ballistic performance of bi-layer ceramic-metal armor plates. And a numerical technique was also proposed, with the effectiveness of simulation results validated by experimental measurements. The penetration process, damage evolution, and underlying mechanisms were systematically explored.

2. Experiments

2.1 Specimen fabrication

The fabrication process for prestressed ceramic-metal composite armor consists of four steps, as shown in Fig. 1. Prestress of circular ceramic disc was exerted by a shrink-fit steel sleeve whose inner diameter was slightly smaller than that of the ceramic. To ensure good assembly of the ceramic disc and the steel sleeve, a fine grinding operation was performed on the contact surface between the two. Upon heating the steel sleeve to 600-850°C in furnace for thermal expansion, the ceramic disc at ambient temperature was rapidly inserted into the sleeve, as shown in Figs. 1(a-b). Upon cooling, the sleeve started to compress the ceramic, generating thermal stresses (prestress) in the ceramic; Fig. 1(c). At the last step (Fig. 1(d)), to construct prestressed bi-layer ceramic-metal armors, the shrink-fit ceramic-steel assembly was bonded to a thin aluminum alloy back plate with epoxy (Loctite Hysol E-120HP).

AD995 alumina (Al_2O_3 , density of 3.89 g/cm³) cylindrical discs were selected,

with $D_c = 50$ mm in diameter and $T_s = 6$ mm in thickness. The sleeves were made of AISI 4340 steel, with an external diameter $D_s = 80$ mm. The back plate was made of aluminum alloy 2024-T3, with thickness $T_b = 3$ mm. Let δ denote the misfit between the diameter of ceramic disc and the inner diameter of sleeve. Table 1 listed the mechanical properties of all the materials used.

To ensure sufficient prestress was applied to the ceramic disc, the method of shrink-fit was adopted. Three types of target plate were prepared for impact experiments: type A without sleeve confinement for none prestress case, type B with 0.11 mm misfit for medium prestress case (125 MPa), and type C with 0.21 mm misfit for large prestress case (274 MPa), as shown in Table 2.

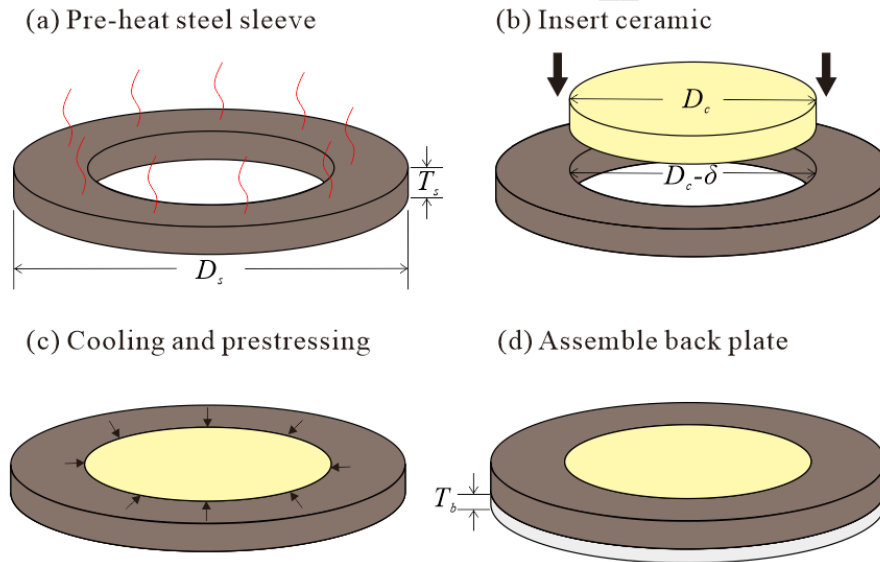


Fig. 1 Shrink-fit assembly of prestressed ceramic-metal composite target

Table 1 Material properties

| Material | Density (g/cm ³) | Elastic modulus (GPa) | Poisson ratio | Yield strength (MPa) |
|--------------------------------|---------------------------------|--------------------------|---------------|-------------------------|
| Al ₂ O ₃ | 3.89 | 370 | 0.22 | - |
| Al 2024-T3 | 2.78 | 72 | 0.33 | 369 |
| AISI 4340 | 7.83 | 200 | 0.30 | 785 |

Table 2 Summary of target plates

| Target | T_s (mm) | D_c (mm) | D_s (mm) | δ (mm) | T_b (mm) | q (MPa) |
|--------|------------|------------|------------|---------------|------------|-----------|
| A | 6 | 50 | - | - | 3 | 0 |
| B | 6 | 50 | 80 | 0.11 | 3 | 125 |
| C | 6 | 50 | 80 | 0.21 | 3 | 274 |

2.2 Analytical prediction and measurements of the prestress

For the problem considered in the current study, the ceramic disc can be considered as an elastic cylinder with pressure q exerted on its radial boundary. Due to axisymmetry, the stress state in the ceramic disc is uniform and obeys:

$$\sigma_r = \sigma_\theta = q \quad (2)$$

where σ_r and σ_θ are the normal stresses along radial and circumferential directions. The steel sleeve can be considered as an elastic-perfectly-plastic circular ring with internal pressure q . By solving this boundary value problem and assuming the steel sleeve remains elastic, the prestress (or pressure q) can be analytically calculated as:

$$q = \frac{\frac{\delta}{D_c}}{\frac{(1+\nu_c)(1-2\nu_c)}{E_c} + \frac{(1+\nu_s)}{E_s \left(\left(\frac{D_s}{D_c} \right)^2 - 1 \right)} \left[(1-2\nu_s) + \left(\frac{D_s}{D_c} \right)^2 \right]} \quad (3)$$

When the maximum stress in the sleeve exceeds the yielding stress (σ_y) of steel, the prestress is given as [20, 21]

$$q = \sigma_y \left(\ln \frac{D}{D_c} + \frac{D_s^2 - D^2}{2D_s^2} \right) \quad (4)$$

where D is the diameter of the elastic-plastic boundary in the sleeve cross-section. D can be calculated from the following equation:

$$\begin{aligned} \frac{\delta}{D_c} = & (1-2\nu_s)(1+\nu_s) \frac{\sigma_y}{E_s} \left[\ln \left(\frac{D_c}{D} \right) + \frac{1}{2} \left(\frac{D}{D_s} \right)^2 - \frac{1}{2} \right] \\ & + (1-\nu_s^2) \frac{\sigma_y}{E_s} \left(\frac{D}{D_c} \right)^2 + (1-\nu_c) \frac{\sigma_y}{E_c} \left[\ln \left(\frac{D}{D_c} \right) + \frac{1}{2} - \frac{1}{2} \left(\frac{D}{D_s} \right)^2 \right] \end{aligned} \quad (4)$$

where (E_c, E_s) and (ν_c, ν_s) are the elastic modulus and Poisson ratio of ceramic and steel, respectively.

Experimentally, the prestress can be measured by X-ray diffractometer (XRD),

which allows non-destructive determination of residual stresses in polycrystalline materials. As prestress changes interplanar crystal spacing, the diffraction peak of XRD varies when the level of prestress is altered. By collecting the XRD patterns at different incident angles ψ , the prestress can be measured [22, 23]. In the present study, the measurements were conducted with Bruker D8 ADVANCE. Figure 2(a) plotted the angel of diffraction peak 2θ as a function of $\sin^2\psi$. The thus measured normal stresses at the center points of ceramic surfaces in type B and C targets were 125 MPa and 274 MPa, respectively (Table 2). Figure 2(b) and Table 3 compared the analytically predicted prestresses with those measured experimentally for selected misfit sizes. Good agreement is achieved.

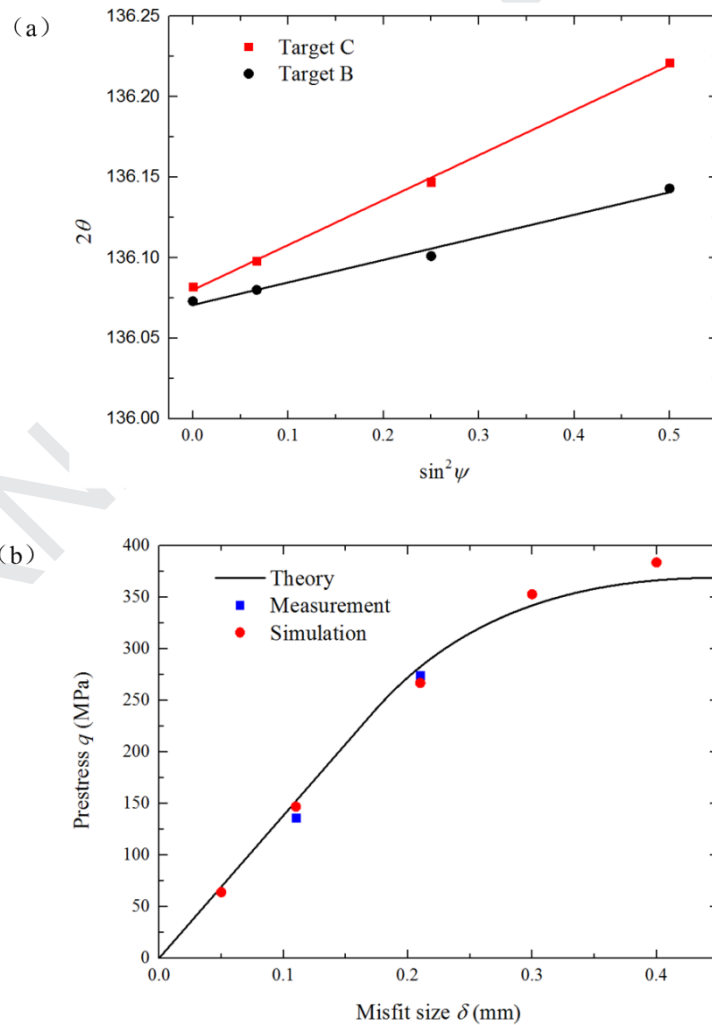


Fig. 2 (a) The angel of diffraction peak 2θ as a function of $\sin^2\psi$; (b) Prestress q verves misfit size δ in diameter.

Table 3 Prestress levels at different misfits.

| Misfit (mm) | Prestress (MPa) | | |
|-------------|-----------------|-------------|---------------|
| | Theory | Measurement | FE simulation |
| 0.05 | 69 | - | 64 |
| 0.11 | 152 | 136 | 147 |
| 0.21 | 282 | 274 | 267 |
| 0.30 | 342 | - | 353 |
| 0.40 | 366 | - | 384 |

2.3 Ballistic tests

Ballistic tests were performed using a two-stage light gas gun. High purity nitrogen was compressed to accelerate the projectiles, and velocities up to 900 m/s could be reached. The projectiles were AISI 4340 steel cylinders with diameter 7.62 mm, length 20 mm, and mass 7.1 g. As shown schematically in Fig. 3(a), the boundary of each target plate was clamped by the clamping plates. More details of the clamping arrangement were presented in Fig. 3(c). The diameter (D_h) of the inner hole in each clamping plate was 60 mm.

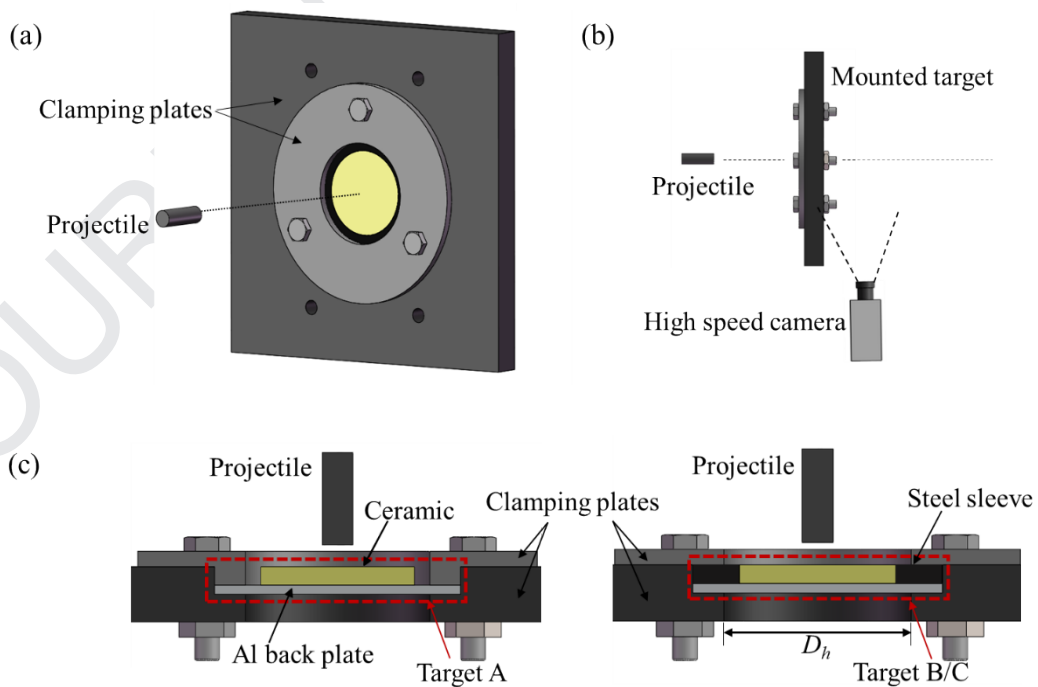


Fig. 3 (a) Schematic of target supported by clamping plates and impacted by projectile. (b) Schematic of high speed camera used to obtain residual velocity. (c) Cross section of the clamping arrangement for Targets A, B and C.

Impact velocities were measured using three laser gates before the target. As shown in Fig. 3(b), a I-Speed 716 high-speed camera was employed to capture the dynamic deformation process of the Al back plate and to measure the residual velocity of the projectile if it pierced through the target. The time when the projectile initially contacts with the surface of the ceramic was defined as zero. The exposure time was fixed at 2 μs and the inter-frame interval was 10 μs .

2.4 Experimental results

The targets were impacted at velocities ranging from 300 m/s to 600 m/s. For all three types of target (Table 2), Table 4 listed the results obtained for the impact velocity V_i , the residual velocity V_r and the residual length L_r of projectile. Figure 4 plotted the residual velocity as a function of initial impacting velocity for three prestress levels: 0 MPa, 125 MPa, and 274 MPa. Introducing prestress into the ceramic enabled the residual velocity of projectile to decrease and the ballistic limit of the proposed bi-layer composite armor to increase, and the enhancement was more pronounced at larger prestress levels. As an example, the residual velocities of target A, B, C, impacted by a projectile having an initial impacting velocity of ~ 500 m/s, were 191 m/s, 112 m/s and 0 m/s, respectively. The ballistic limit of target C exceeded 500 m/s, about 25% higher than that of target A.

Table 4 Comparison of ballistic results obtained from simulations and experiments

| Target type | V_i (m/s) | Experiment | | FE simulation | | Error | |
|-------------|-------------|-------------|------------|---------------|------------|---------------|---------------|
| | | V_r (m/s) | L_r (mm) | V_r (m/s) | L_r (mm) | For V_r (%) | For L_r (%) |
| A | 370 | 0 | 17.65 | 0 | 17.20 | 0 | 2.5 |
| | 447 | 96 | 16.84 | 106 | 16.61 | 10.4 | 1.4 |
| | 486 | 152 | 16.51 | 158 | 16.37 | 3.9 | 0.8 |
| | 512 | 191 | 16.10 | 175 | 16.25 | 8.3 | 0.9 |
| B | 394 | 0 | 16.77 | 0 | 16.93 | 0 | 1.0 |
| | 476 | 75 | 16.24 | 66 | 15.99 | 12 | 1.5 |
| | 501 | 112 | 15.80 | 101 | 15.77 | 9.8 | 0.2 |
| | 505 | 117 | - | 106 | 15.74 | 9.4 | - |
| | 580 | 170 | 15.26 | 173 | 15.37 | 1.8 | 0.7 |
| C | 499 | 0 | 15.52 | 0 | 15.58 | 0 | 0.4 |
| | 537 | 32 | 15.24 | 38 | 15.33 | 18.8 | 0.6 |

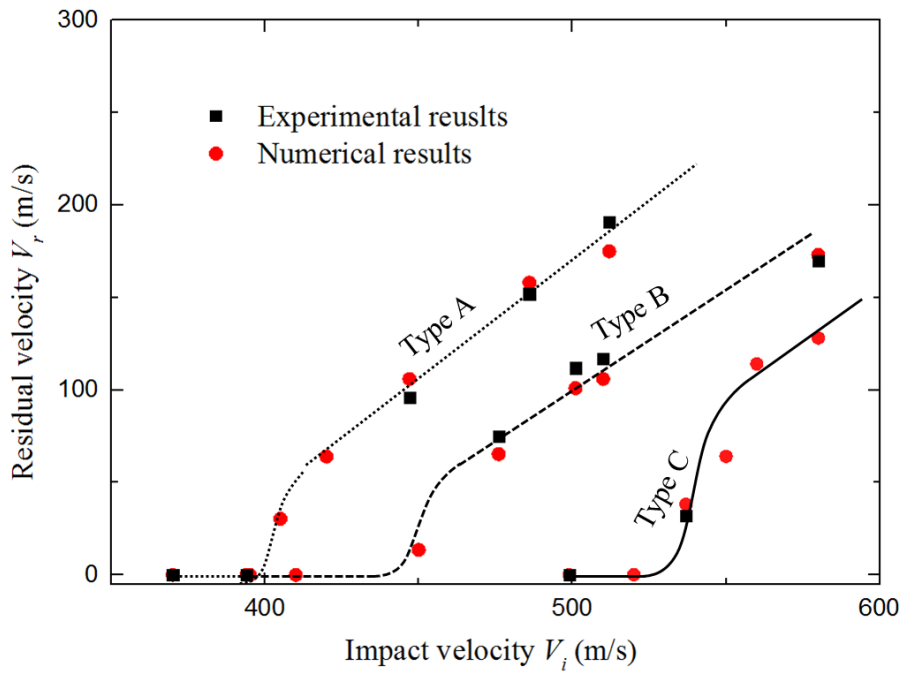


Fig. 4 The residual velocity versus impact velocity at different prestress levels.

A sequence of high-speed images of target A and target C were presented in Figs. 5 and 6, respectively. For target A, once a collision occurred between the projectile and alumina, the latter was comminuted and accelerated. Then the kinetic energy of the ceramic fragments and projectile was transferred to the Al back plate. At $41 \mu\text{s}$, the back plate suffered a significant out-of-plane deflection, leading to a bulge. As time proceeded, the deflection increased and fracture of the back plate eventually occurred. At $111 \mu\text{s}$, white alumina debris began to be emitted from the ruptured back plate. The situation for target C was a bit different from that of target A, as shown in Fig. 6. Whereas the deformation process of Al back plate was similar to that of Fig. 5, the projectile came out with a very low velocity after alumina fragments escaped from the target, causing a maximum displacement of the projectile at $t = 315 \mu\text{s}$. After the ballistic test, it was found that although the Al back plate was almost pierced through its thickness, the projectile was intercepted by the plate, implying that 499 m/s was close to the ballistic limit of target C.

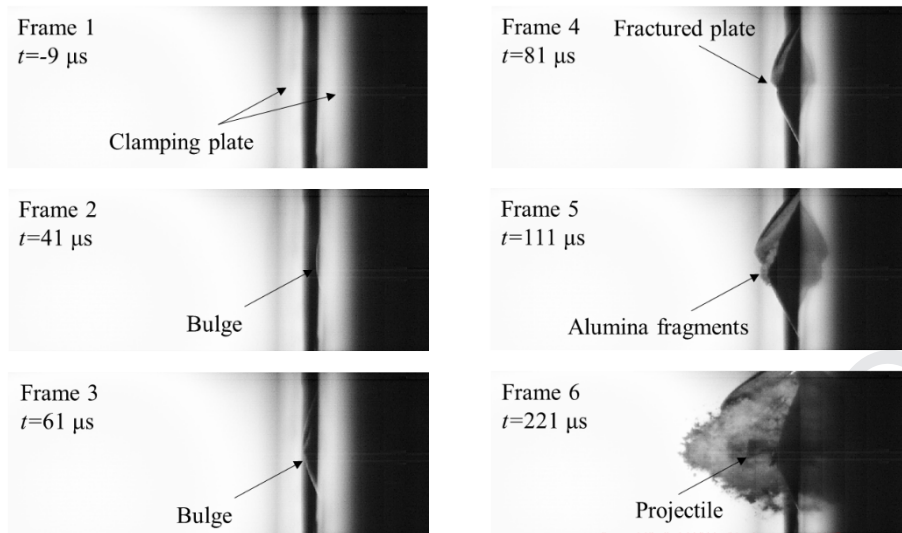


Fig. 5 High-speed image sequence of target A impacted by projectile at 447 m/s.

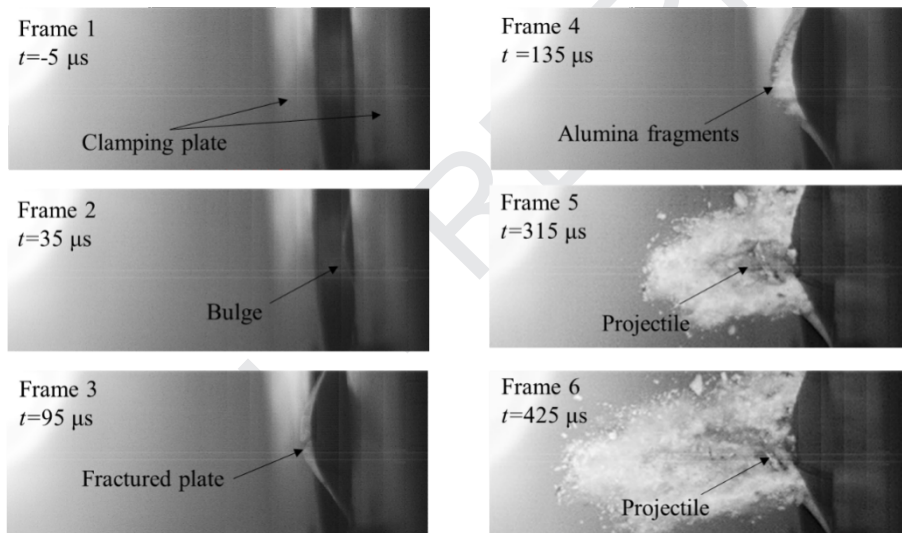


Fig. 6 High-speed image sequence of target C impacted by projectile at 499 m/s.

For target A as shown in Fig. 7(a), the alumina tile was completely fractured and pulverized, with alumina powder, small fragments and large fragments left after the impacts. The powder was generated by the intensive abrasion between projectile and alumina tile, with some small fragments ejected from the impact zone during the penetration. Large fragments might be caused by the combination of bending deformation, and the propagating of both the radial and circumferential cracks. A bulge with the diameter of 60 mm was formed in the back Al plate, presenting a typical dishing deformation and petaling failure. For targets B and C, the damage of ceramic was reduced significantly, as shown in Fig. 7(c) and (e). A circular hole with the diameter of 11 mm formed on the front surface of tile, and a conoid crater

appeared along the axis from the front surface to the rear one. The edge of ceramic was still intact, large fragments were prohibited, and the deformation of back Al plate was less serious than that of target A. This implies that the applied prestress exerted by the shrink fit could reduce the damage of targets.

The projectiles after impact were collected to measure the residual lengths, which were listed in Table 4. It can be demonstrated from the shape of projectiles after impact as shown in Fig. 7 that the projectiles deformed by mushrooming and exhibited a ductile failure. The erosion of projectile could always be observed whether the projectile velocity is higher or lower than the ballistic limit, and the breaking of projectile didn't happen within the velocity range in experiments. It was obvious from Table 4 that the residual lengths of the projectiles were influenced by both prestress and impact velocity. Larger prestress and higher impact velocity resulted in shorter projectile. It can be inferred that prestress can enhance the abrasion between ceramic and projectile, and lead to more energy dissipation by the deformation and the erosion of projectile, which is regarded as the most effective way in energy dissipation of armor designs.

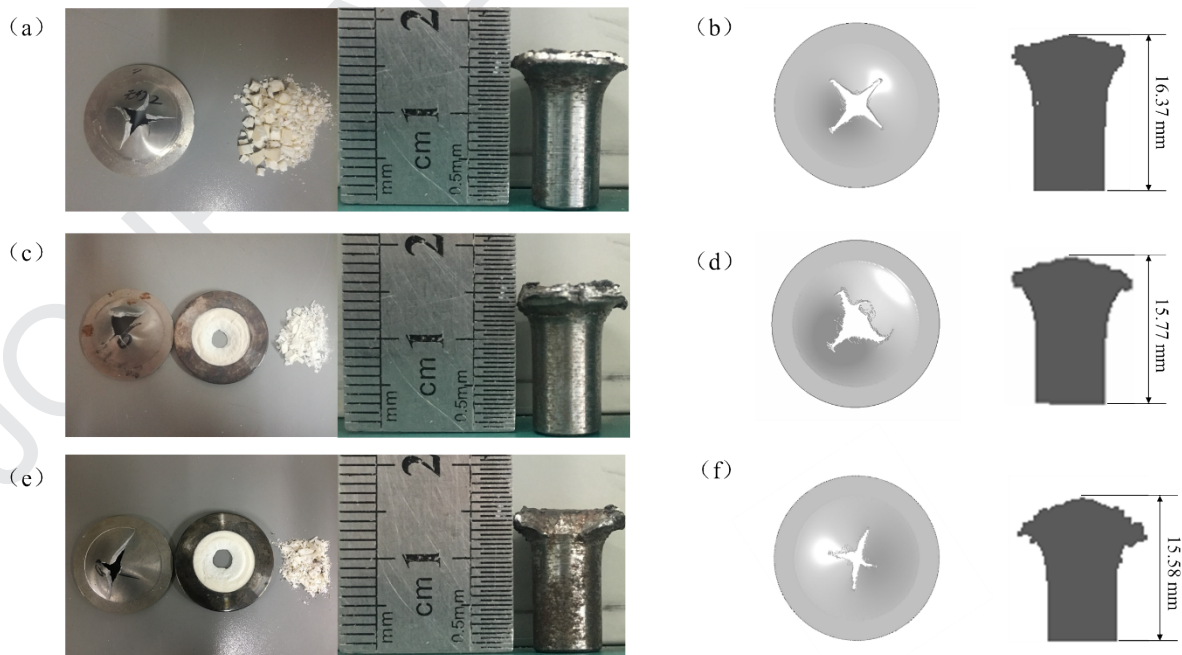


Fig. 7 Failure modes of target plates and corrosion of projectiles after perforation. (a), (b) Target A impacted by projectile at 486 m/s; (c), (d) Target B impacted by projectile at 501 m/s; (e), (f) Target C impacted by projectile at 499 m/s. (a), (c), (d) were from tests; while (b),

(d), (f) were from FE calculations.

3. Simulations

3.1 Numerical models

Numerical simulations based upon the finite element method (FEM) were performed with commercial software LS-DYNA. Full three-dimensional (3D) model for each type of target was built, as shown in Fig. 8. The steel sleeve and back Al plate were meshed using element SOLID 164 based upon the Lagrangian algorithm. The projectile was modeled by employing the method of smooth partial hydrodynamics (SPH), since this method has no grid restriction and thus can avoid mesh distortions in large deformation.

The prestressed ceramic was divided into two parts, *i.e.*, the central ceramic with a diameter of 40 mm modeled by SPH, and the side ceramic ring modeled by FEM. The reason for using SPH for the central ceramic was: deletion of distorted elements in FEM would lead to zero-pressure voids and cause the loss of confinement pressure; in comparison, the SPH method has the advantage of reproducing the pulverization and fragmentation of ceramic, thus more reasonable for the impact contact area [24]. For the side ceramic ring, FEM was used to model the shrink-fit so that prestressing could be exerted on the ceramic, as discussed in detail in Subsection 3.3. To ensure integrity, the nodes of smoothed particles for the central ceramic region were tied with those of the elements for the side ceramic ring at the interface.

The size of finite elements was 1 mm for steel sleeve, 0.7 mm for side ceramic ring, and 0.5 mm for back Al plate. The size of SPH particles was 0.5 mm for both central ceramic and projectile. Selection of these mesh sizes was a compromise between the convergence of numerical simulations and computational cost.

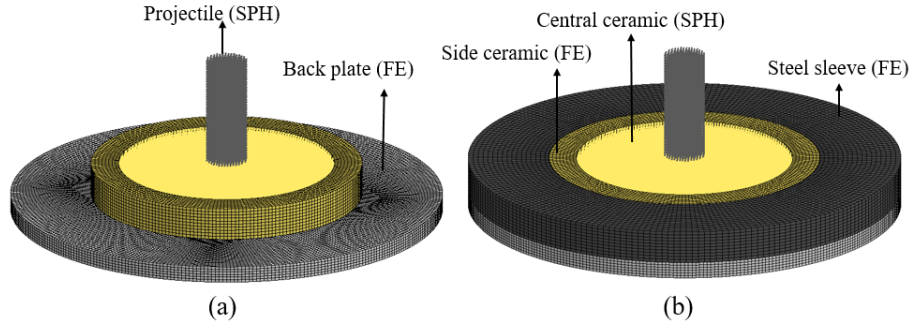


Fig. 8 Full three-dimensional models for target (a) A, (b) B and C.

3.2 Material models and constants

The Johnson-Cook constitutive and failure models were employed for AISI 4340 steel sleeve [25] and aluminum alloy 2024-T3 [26], with material parameters as listed in Table 5. For ceramic (AD995 alumina) tiles, the Johnson–Holmquist–2 constitutive relation and damage criterion were adopted, and relevant parameters taken from [27] were listed in Table 6. The hydrostatic tensile limit T was modified slightly from 0.262 GPa to 0.312 GPa.

Table 5 Material parameters for AISI 4340 steel [25] and aluminum alloy 2024-T3 [26]

| Material/Constants | Steel 4340 | Al 2024-T3 |
|--|------------|------------|
| Density, ρ (kg/m ³) | 7.83 | 2.78 |
| Shear modulus, G (GPa) | 77 | 27 |
| Bulk modulus, K_1 (GPa) | 159 | 77 |
| Static yield strength, A (GPa) | 0.785 | 0.369 |
| Strain hardening constant, B (GPa) | 0.510 | 0.684 |
| Strain hardening exponent, n | 0.260 | 0.73 |
| Strain rate constant, C | 0.014 | 0.0083 |
| Thermal softening exponent, m | 1.03 | 1.7 |
| Reference strain rate, $\dot{\epsilon}_0$ (s ⁻¹) | 1.0 | 1.0 |
| Melting temperature, t_m (K) | 1793 | 893 |
| Specific heat, C_r (J/Kg·K) | 477 | 875 |
| Damage constant, d_1 | 0.05 | 0.112 |
| Damage constant, d_2 | 3.44 | 0.123 |

| | | |
|------------------------|-------|-------|
| Damage constant, d_3 | -2.12 | 1.5 |
| Damage constant, d_4 | 0.002 | 0.007 |
| Damage constant, d_5 | 0.61 | 0 |

Table 6 Material parameters for AD995 alumina ceramic [27]

| Parameters | Value |
|---|-------|
| Density, ρ (kg/m ³) | 3.89 |
| Shear modulus, G (GPa) | 152 |
| Pressure constant, K_1 (GPa) | 231 |
| Pressure constant, K_2 (GPa) | -160 |
| Pressure constant, K_3 (GPa) | 2774 |
| Bulking factor, β | 1.0 |
| Hugoniot elastic limit (<i>HEL</i>) (GPa) | 6.57 |
| Intact strength constant, A | 0.88 |
| Intact strength constant, N | 0.64 |
| Strain rate constant, C | 0.07 |
| Fracture strength constant, B | 0.28 |
| Fracture strength constant, M | 0.6 |
| Hydrostatic tensile limit, T (GPa) | 0.312 |
| Damage constant, D_1 | 0.01 |
| Damage constant, D_2 | 0.7 |

3.3 Prestress modeling

For the present numerical simulations, prestressing in the model was achieved through the contact between side ceramic and sleeve using the keyword CONTACT_SURFACE_TO_SURFACE_INTERFACE. The initial diameter of ceramic disc was set larger than the inner diameter of steel sleeve. The contact type adopted could turn off the checking of nodal interpenetrations at the starting of simulation and introduce a dynamic relaxation phase to calculate the prestress before the calculation of projectile penetration [28]. During the initial stage of dynamic relaxation, the contact stiffness between the ceramic and the sleeve was gradually

increased, resulting in increased interface stresses; meanwhile, the overlap gradually disappeared, as shown in Fig. 9. As soon as the overlap completely disappeared, numerical convergence was achieved and the prestress state in the ceramic was stabilized. Once the dynamic relaxation phase stopped, the calculation of penetration process started from the preloaded state automatically. The prestress calculated from the numerical simulations was quite uniform in the ceramic disc, and good agreement among FEM simulations, XCT measurements and analytical predictions was achieved (Table 3). In the case of large-size misfit, the small deviations of analytical predictions from FEM calculations were mainly attributed to the strain hardening of steel sleeve in prestress modeling.

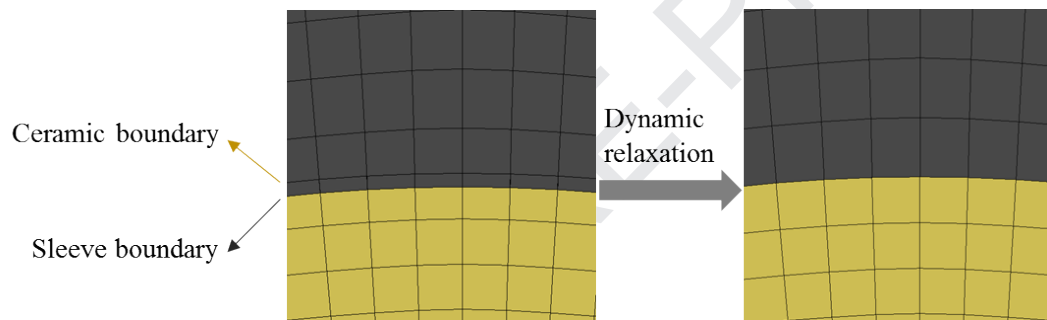


Fig. 9 Mesh at ceramic-sleeve interface and removal of overlap after dynamic relaxation.

3.4 Verification and discussions

3.4.1 Validation of numerical simulation

Numerical and experimental results for the three target types were presented in Fig. 4, while quantitative comparison between the two was given in Table 4. While the percentage errors appeared to be relatively large for the residual velocity of projectile, the deviations were less than 20 m/s in absolute value, even for residual velocity exceeding 100 m/s. As for the residual length of projectile, the percentage errors were less than 3%. Moreover, as shown in Fig. 7, the numerically calculated failure mode of Al back plate as well as post-impact shape of projectile agreed fairly well with those from experiments. Therefore, the feasibility and validity of numerical models developed in the present study was established.

3.4.2 Penetration process

Figure 10(a) plotted the computed projectile velocity as a function of time for all three targets at an impact velocity of 500 m/s, from which the penetration process could be divided into three phases. Taking target C as an example: at Phase 1, the velocity dropped sharply to 430 m/s within the first 1.5 μs ; the duration of Phase 2 was about 20 μs , and the curve was flat at the beginning of this phase and then descended rapidly; at Phase 3, the velocity gradually reduced to zero in about 150 μs , implying that the projectile was completely intercepted.

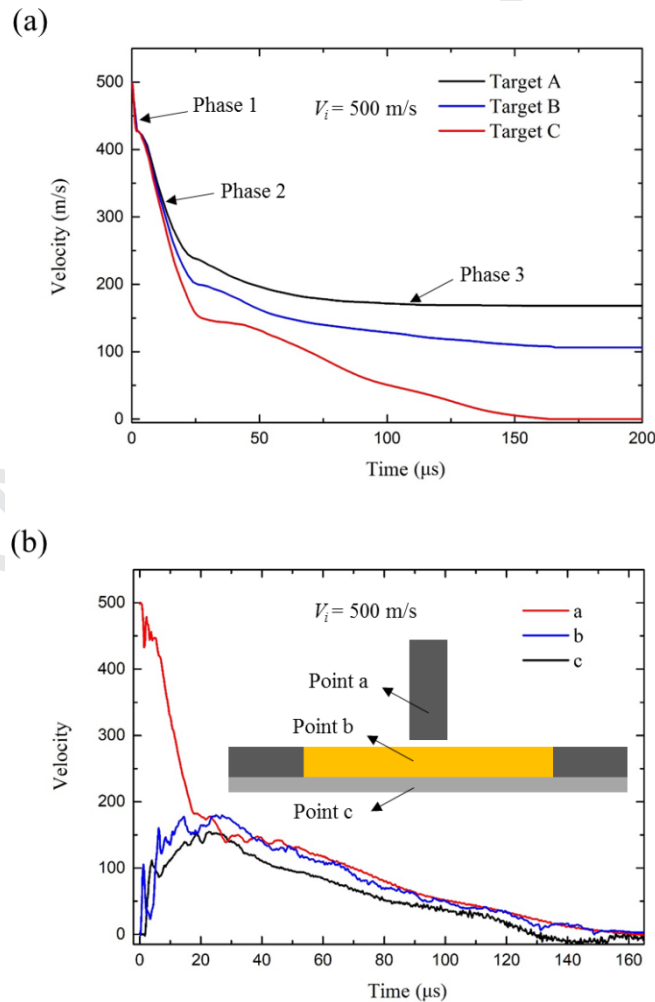


Fig. 10 (a) Velocity histories of projectile for targets A, B and C and (b) velocity histories of three representative points in target C at initial impact velocity of 500 m/s.

To further explore the penetration mechanism, representative points in the

projectile, the ceramic and the Al back plate were selected, and the velocity history of each point was presented in Fig. 10(b). Damage contours of the ceramic at different time steps after projectile impact were displayed in Fig. 11 for all three target types. In the first microsecond, damage was initiated from both the front and rear surfaces of ceramic, causing a cone crack to form. The projectile was unable to penetrate the ceramic, since the damage zone was below a critical size: as a result, the projectile was severely eroded at the front surface of ceramic and its velocity dropped sharply, known as dwelling [29]. Damage on the front surface of ceramic was caused by the great pressure generated by the impact contact of projectile. Damage on the rear surface of ceramic was caused by tensile wave reflected from the interface between ceramic and Al back plate. Damage on the rear surface propagated towards the front surface rapidly, reaching the front surface at $t = 1.5 \mu\text{s}$. By then, most ceramic beneath the projectile had failed and penetration of projectile was initiated.

At the beginning of second phase, a cone crack was developed towards the rear surface of ceramic due to large compressive stress, and the extent of damage on the rear surface increased as well. When the cone crack reached the rear surface, a ceramic conoid was formed. Inside the conoid, most of the ceramic was comminuted and the corresponding SPH nodes were fully damaged. Since the conoid was still supported by the Al back plate, it helped to redistribute the impact load to a larger region of the back plate surface. Afterwards, the projectile penetrated and accelerated the conoid, transforming the ballistic energy to the kinetic energy of both ceramic conoid and the back plate. Figure 10(b) showed the difference between the second and third phases. The remained ceramic conoid and the central portion of the back plate were accelerated, with their velocities approaching that of the projectile at about $25 \mu\text{s}$, which implied the penetration of projectile into the ceramic conoid had stopped.

Subsequently, the projectile, the ceramic conoid and the back plate moved forward as an aggregation, with the resistance to projectile mainly contributed by the plastic deformation of the back plate, leading to the gentle decrease of projectile velocity in phase 3 as shown in Fig. 10(a).



















| Phase | Time | Target A | Target B | Target C |
|-------|----------------------|--|---|--|
| | | $V_i = 500 \text{ m/s}$ | | |
| 1 | 1.00 μs |  |  |  |
| | 1.25 μs |  |  |  |
| 2 | 2.00 μs |  |  |  |
| | 4.00 μs |  |  |  |
| 3 | 25.00 μs |  |  |  |
| | 100.00 μs |  |  |  |

Fig. 11 Numerically simulated evolution of damage in targets A, B and C subjected to projectile impact at 500 m/s.

3.4.3 Mechanisms of prestress

The results shown in the previous section revealed that, during the first phase, prestress played an insignificant role and the velocity of projectile reduced to 430 m/s for all the three targets. This observation is different from existing studies [18, 19], which concluded that prestressing led to increased dwell time. The discrepancy is mainly attributed to two reasons. On one hand, the ceramic used in the current study was thin alumina, not the thick silicon carbide used in [18, 19]. On the other hand, the impedance of Al back plate is much smaller than that of alumina, resulting in more intensive reflected tensile wave. The lower tensile strength of alumina, the smaller thickness, and the larger impedance mismatch at the interface all led to fast accumulation of damage on the rear surface of alumina disc. The duration of interface dwell was almost the same for all three targets at different impact velocities in simulations. Therefore, the dwell time is too short to be influenced by prestress.

However, for thick silicon carbide tile supported by steel, the damage on its rear surface is much milder and the dwell time is in tens of microseconds. This implies that the dwell time of thick silicon carbide is mainly determined by ceramic compressive strength, which can be enhanced by prestress. Moreover, according to existing experimental data [30], the strength of intact silicon carbide is more sensitive to pre-pressure than that of intact alumina. Consequently, the effect of prestress on ballistic performance may be more significant in thick silicon carbide than that in thin alumina.

As illustrated in Fig. 11, the prestressed targets at 4 μs and 25 μs exhibited much less damage than the target without prestress. Different from the situation in the first phase, the prestress had a significant effect on compressive damage in the second phase. For the prestressed targets, the initiation and propagation of crack was suppressed, since the ceramic was relatively intact and stronger to provide greater resistance. Moreover, the damage was restricted to a smaller region, and the damaged ceramic was confined by the surrounding ceramic. Thus, subsequent movement of ceramic fragments was constrained, and the fragments were continually forced to rub with the projectile. For the prestressed targets, the decrease in velocity during the second phase was steeper (Fig. 10(a)), while the duration was slightly increased. At the end of the second phase, the difference in projectile velocity between target A (no prestress) and C (274 MPa prestress) was almost 90 m/s.

When impact contact occurred between the projectile and the target, the target material just ahead of the projectile deformed more in the out-of-plane direction than the material away from the impact zone, due to inertia effects [31]. This caused the ceramic tile to bend slightly. At the third phase, bending effect was apparent for target A. Circumferential cracks and radial cracks caused by high tensile stress could be found outside the ceramic conoid, disintegrating the ceramic into large fragments. In contrast, for the prestressed targets, circumferential cracks and radial cracks were effectively suppressed, while the ceramic at the lateral boundary remained intact. At the end of third phase, targets A and B were both perforated by the projectile.

However, target C with a relatively large prestress (274 MPa) successfully intercepted the projectile.

Figure 12 compared the energy absorption between targets A and C at impact velocity 500m/s, with a total initial kinetic energy of 887.5J. The kinetic energy was mainly dissipated by plastic deformation and erosion of projectile within the first two phases, *i.e.*, the initial 20 μ s. During the third phase, the resistance provided by the ceramic was insufficient to further deform the projectile while the internal energy of projectile remained constant. Prestress enabled the projectile to experience more serious erosion, causing the energy dissipation to increase by 12% relative to that of target A. The final energy absorptions by the ceramic and the Al back plate were almost the same. The internal energy of ceramic had a slight decrease at 1 μ s, corresponding to the initiation of damage in the ceramic. Besides, for target C, the internal energy of ceramic was slightly higher, due likely to the enhanced compressive strength of ceramic in the prestressed state.

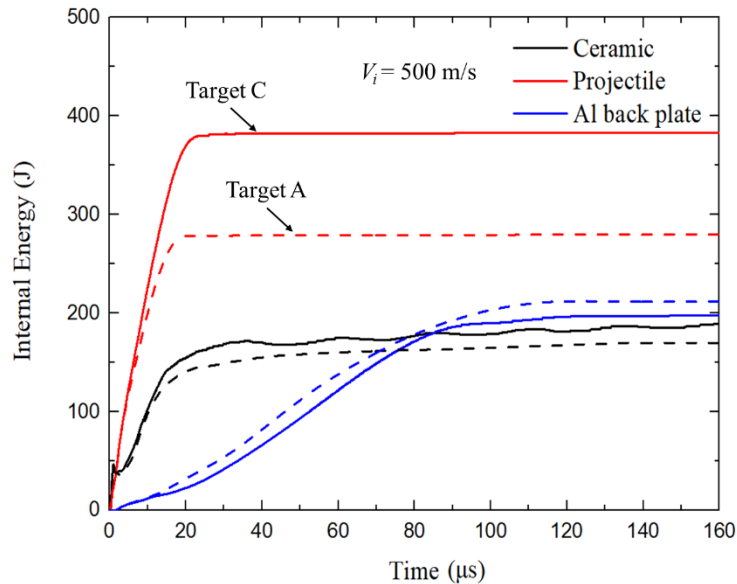


Fig. 12 Effect of prestress on energy absorbed by constituting components at initial impact velocity of 500 m/s. Dash lines corresponded to target A (no prestress), while solid lines referred to target C (274 MPa prestress)

3.4.4 Influence of ceramic size

Additional numerical simulations were carried out to explore how the thickness and diameter of ceramic disc affected the ballistic limit of bi-layer composite targets. The results were presented in Fig. 13, with the target without prestress compared to that with prestress. For all the simulations, the thickness of the Al back plate was fixed to 3 mm. For the prestressed target, the misfit between the ceramic disc and the steel sleeve was adjusted to provide a prestress of 270 MPa.

With reference to Fig. 13(a), to quantify the influence of ceramic thickness, the diameter of ceramic disc was fixed at 50 mm. When the ceramic thickness was less than 5 mm, prestress almost had no effect on ballistic performance. As the thickness of ceramic exceeded 5 mm, the enhancement effect of prestress became more obvious: the ballistic limit was elevated by more than 100 m/s when the thickness exceeded 6 mm. This was attributed to two factors. First, thin ceramic disc was more sensitive to tensile damage initiated from the interface and hence suffered more tensile damage. Second, the duration of second phase was shorter for thinner ceramic discs, as there was less mass beneath the projectile to be penetrated and accelerated. The result implied that, to design an armor system against specific threat, the benefit of prestress is appreciated only when the thickness of ceramic exceeds a critical value.

To quantify the influence of ceramic diameter, the thickness of ceramic was fixed at 6 mm. From Fig. 13(b) it was seen that the ballistic performance of bare ceramic disc (with no prestress) was strongly affected by ceramic diameter smaller than 50 mm, while the influence vanished for ceramic diameter larger than 50 mm. The ballistic limit increased from 295 m/s to 400 m/s as the diameter increased from 30 mm to 50 mm, which was attributed to the tensile wave initiated from the lateral free boundary of ceramic without any confinement. The tensile stress wave reflected from the boundary would cause the collapse of ceramic, and hence a ceramic disc with small diameter was more likely to be damaged by the tensile wave. In particular, the ceramic disc with diameter 30 mm was fully fragmentized and would be pushed away by the projectile during penetration, leading the reduction of its resistance. In contrast,

for a prestressed target, irrespective of ceramic disc diameter, the confinement of steel sleeve and the prestress of ceramic could provide sufficient confinement and eliminate the tensile wave as much as possible. As a result, there was much less dependence of ballistic limit on ceramic disc diameter, as shown in Fig. 13(b).

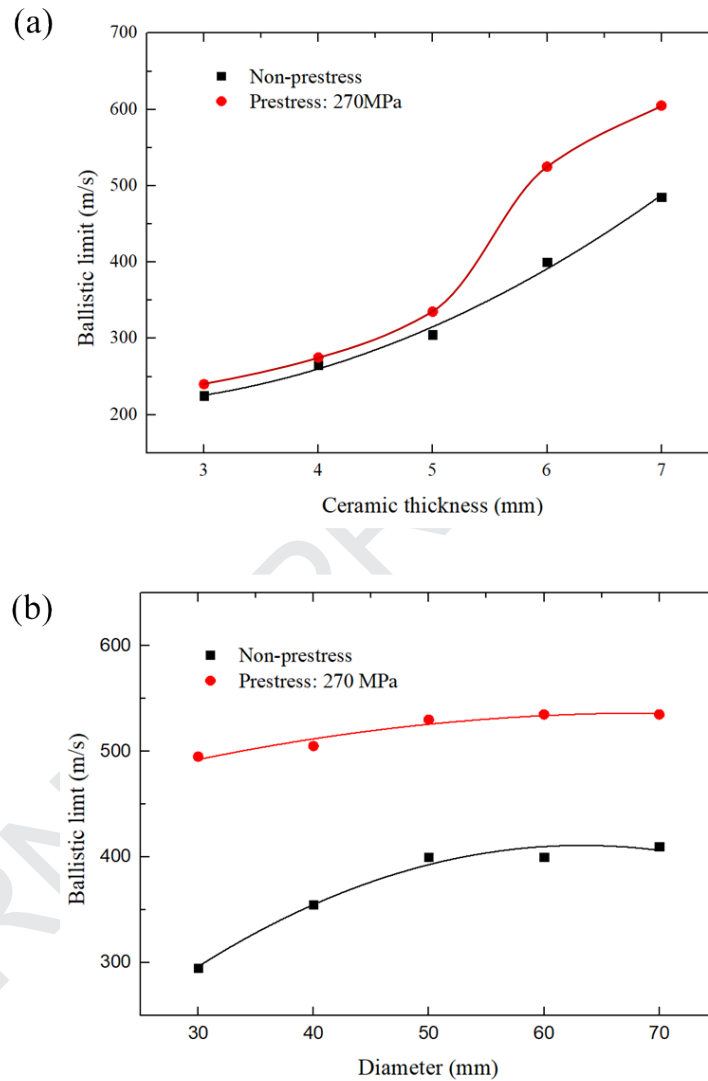


Fig. 13 Effects of ceramic disc (a) thickness and (b) diameter on ballistic limits of bi-layer composite targets with and without prestress.

4. Concluding remarks

A combined experimental and numerical approach was employed to investigate the ballistic performance of alumina tiles having controlled prestress. Three types of

bi-layer ceramic composite plate with different prestress levels were prepared using the method of shrink-fit, and tested with ballistic experiments. The influence of prestress on ballistic limit was quantified. Main conclusions are summarized as follows:

- (1) Prestress efficiently improved the ballistic performance of bi-layer ceramic composite armors, and the effect was more pronounced for larger prestress levels. In contrast to a target plate with no prestress, the target with large prestress always exhibited a larger ballistic limit (increased more than 25%) and a smaller residual projectile length, for the steel projectile was more seriously eroded.
- (2) The penetration process of projectile could be divided into three phases: a short dwell phase as the first phase, the second phase within which the ceramic conoid was penetrated and accelerated by the projectile, and the third phase during which the residual kinetic energy of projectile was mainly absorbed by the deformation of the back plate.
- (3) For bi-layer ceramic composite armors, the enhancement of ballistic limit by prestress was mainly attributed to the interaction between ceramic and projectile during the second phase, which resulted in more kinetic energy dissipated by both the deformation and erosion of the projectile itself.
- (4) The effect of prestress on ballistic limit exhibited less dependence on the diameter of ceramic tile, but was significantly dependent upon its thickness.

Indeed, the present work shows prestressing is an effective way to improve ballistic performance of ceramic armor under a specific thickness, which is an important design factor in some armor applications. Further, the experimental results imply that the damage in ceramic can be significantly reduced and the multi-hit ability of ceramic armor can be achieved. However, the steel sleeve may not be the most suitable candidate for optimal weight solution. In this case, aluminum or titanium could be better as the metal sleeve to apply the prestress.

Acknowledgments

This work was supported by the National Natural Science Foundation of China (11802221, and 11472208), the National Key R&D Program of China (2018YFB1106400), China Postdoctoral Science Foundation (2016M600782), Postdoctoral Scientific Research Project of Shaanxi Province (2016BSHYDZZ18), Zhejiang Provincial Natural Science Foundation of China (LGG18A020001), Natural Science Basic Research Plan in Shaanxi Province of China (2018JQ1078).

References

- [1] Wilkins ML. Mechanics of penetration and perforation . *International Journal of Engineering Science*. 1978;16:793-807.
- [2] Gama BA, Bogetti TA, Fink BK, Yu CJ, Claar TD, Eifert HH, et al. Aluminum foam integral armor: a new dimension in armor design. *Composite Structures*. 2001;52:381-95.
- [3] Shokrieh MM, Javadpour GH. Penetration analysis of a projectile in ceramic composite armor. *Composite Structures*. 2008;82:269-76.
- [4] Gamble EA, Compton BG, Deshpande VS, Evans AG, Zok FW. Damage Development in an Armor Ceramic Under Quasi-Static Indentation. *Journal of the American Ceramic Society*. 2012;94:s215-s25.
- [5] Han B, Zhang ZJ, Zhang QC, Zhang Q, Lu TJ, Lu BH. Recent advances in hybrid lattice-cored sandwiches for enhanced multifunctional performance. *Extreme Mechanics Letters*. 2016;10.
- [6] Guo X, Sun X, Tian X, Weng GJ, Ouyang QD, Zhu LL. Simulation of ballistic performance of a two-layered structure of nanostructured metal and ceramic. *Composite Structures*. 2016;157:163-73.
- [7] An X, Yang J, Tian C, Wang B, Guo H, Dong Y. Penetration resistance of hybrid metallic honeycomb structures with ceramic insertions against long-rod tungsten projectiles. *Composite Structures*. 2018;189.
- [8] Jiao WJ, Chen XW. Approximate solutions of the Alekseevskii–Tate model of long-rod penetration. *Acta Mechanica Sinica*. 2018:1-15.
- [9] Heard HC, Cline CF. Mechanical behaviour of polycrystalline BeO, Al₂O₃ and AlN at high pressure. *Journal of Materials Science*. 1980;15:1889-97.
- [10] Hu G, Ramesh KT, Cao B, McCauley JW. The compressive failure of aluminum nitride considered as a model advanced ceramic. *Journal of the Mechanics and Physics of Solids*. 2011;59:1076-93.
- [11] Chen W, Ravichandran G. Failure mode transition in ceramics under dynamic multiaxial compression. *International Journal of Fracture*. 2000;101:141-59.
- [12] Sherman D, Ben-Shushan T. Quasi-static impact damage in confined ceramic tiles. *International Journal of Impact Engineering*. 1998;21:245-65.
- [13] Pickering EG, O'Masta MR, Wadley HNG, Deshpande VS. Effect of confinement on the static and dynamic indentation response of model ceramic and cermet materials. *International Journal of*

Impact Engineering. 2017;110:123-37.

[14] Gassman AH, Paris V, Levin L, Asaf Z, Ya'Akobovich A, Ran E, et al. Effect of Prestressing on the Ballistic Performance of Alumina Ceramics: Experiments and Modeling: John Wiley & Sons, Inc., 2013.

[15] Serjouei A, Gour G, Zhang X, Idapalapati S, Tan GEB. On Improving Ballistic Limit of Bi-Layer Ceramic–Metal Armor. *International Journal of Impact Engineering*. 2016;105:54-67.

[16] Lundberg P, Renström R, Lundberg B. Impact of metallic projectiles on ceramic targets: transition between interface defeat and penetration. *International Journal of Impact Engineering*. 2000;24:259-75.

[17] Lundberg P, Renström R, Andersson O. Influence of confining prestress on the transition from interface defeat to penetration in ceramic targets. *Defence Technology*. 2016;12:263-71.

[18] Chi R, Serjouei A, Sridhar I, Geoffrey TEB. Pre-stress effect on confined ceramic armor ballistic performance. *International Journal of Impact Engineering*. 2015;84:159-70.

[19] Holmquist TJ, Johnson GR. Modeling prestressed ceramic and its effect on ballistic performance. *International Journal of Impact Engineering*. 2005;31:113-27.

[20] Chen W, Ravichandran G. Dynamic compressive failure of a glass ceramic under lateral confinement. *Journal of the Mechanics & Physics of Solids*. 1997;45:1303-28.

[21] Shafiq M, Subhash G. Dynamic deformation characteristics of zirconium diboride-silicon carbide under multi-axial confinement. *International Journal of Impact Engineering*. 2016;91:158-69.

[22] Leoni M, Scardi P, Sglavo VM. Relaxation of indentation residual stress in alumina: Experimental observation by X-ray diffraction. *Journal of the European Ceramic Society*. 1998;18:1663-8.

[23] Noyan IC, Cohen JB. *Residual Stress*: Springer-Verlag, 1987.

[24] Bresciani LM, Manes A, Romano TA, Iavarone P, Giglio M. Numerical modelling to reproduce fragmentation of a tungsten heavy alloy projectile impacting a ceramic tile: Adaptive solid mesh to the SPH technique and the cohesive law. *International Journal of Impact Engineering*. 2016;87:3-13.

[25] Johnson GR, Cook WH. Fracture characteristics of three metals subjected to various strains, strain rates, temperatures and pressures. *Engineering Fracture Mechanics*. 1985;21:31-48.

[26] Serjouei A, Chi R, Zhang Z, Sridhar I. Experimental validation of BLV model on bi-layer ceramic-metal armor. *International Journal of Impact Engineering*. 2015;77:30-41.

[27] Krashanitsa RY. An Inverse Computational Approach for the Identification of the Parameters of the Constitutive Model for Damaged Ceramics Subjected to Impact Loading [electronic resource]. 2005. p. 349-57.

[28] Hallquist JO. *LS-DYNA keyword user manual version 971*. 2007.

[29] Li JC, Chen XW, Ning F, Li XL. On the transition from interface defeat to penetration in the impact of long rod onto ceramic targets. *International Journal of Impact Engineering*. 2015;83:37-46.

[30] Bavdekar S, Subhash G. Comparison of pressure-sensitive strength models for ceramics under ultrahigh confinement. *International Journal of Impact Engineering*. 2018;118:60-6.

[31] Chen WW, Rajendran AM, Song B, Nie X. Dynamic Fracture of Ceramics in Armor Applications. *Journal of the American Ceramic Society*. 2010;90:1005-18.